Filtered Kriging for Improved Interpolation of Periodic Manufacturing Surfaces

Zhiqiao Dong[a], Sixian Jia[b], Chenhui Shao[a,b,*]

[a]*Department of Mechanical Science and Engineering, University of Illinois at Urbana-Champaign, Urbana, IL 61801, USA*
[b]*Department of Mechanical Engineering, University of Michigan, Ann Arbor, MI 48109, USA*

Abstract

High-resolution characterization of surfaces is essential in a variety of quality control tasks in modern manufacturing, such as surface quality inspection and tooling maintenance. However, direct high-resolution surface measurements often come with high cost and/or long measurement time. Interpolation based on spatial process models, especially kriging-type methods, has been used to obtain denser estimations from low-resolution and cheaper measurements. Periodic spatial correlations, which commonly exist in manufacturing applications, cannot be adequately captured by conventional spatial models, thereby causing potential performance degradation or numerical issues. To address these challenges, we propose a new procedure termed as filtered kriging (FK), which separates the periodic component using a bandpass pre-filter, such that the residual can be well fitted with common models. Through frequency-domain analysis, conditions under which FK is effective are identified, and a practical bandpass filter design strategy is devised. A new theorem is proven to show that, when measurements are free from aliasing, perfect reconstruction guaranteed by the Nyquist-Shannon sampling theorem is achieved by FK estimations under certain assumptions. Finally, the effectiveness of FK is demonstrated by case studies using real-world periodic surfaces from two-photon lithography and ultrasonic

*Corresponding author
Email addresses: zhiqiao5@illinois.edu (Zhiqiao Dong), sixian@umich.edu (Sixian Jia), chshao@umich.edu (Chenhui Shao)

metal welding. FK is shown to capture spatial correlation more adequately than conventional methods, and achieves better interpolation accuracy.
Keywords: spatial interpolation, periodic surfaces, filtering, two-photon lithography, ultrasonic metal welding, surface metrology

1. Introduction

Fine-scale characterization of surfaces and geometric compliance is crucial for quality control of various manufacturing processes, e.g., machining and micro-machining [1–4], wafer manufacturing [5, 6], ultrasonic metal welding (UMW) [7, 8], two-photon lithography (TPL) [9, 10], additive manufacturing [11, 12], and many others [13–15]. However, high-resolution surface measurements typically rely on expensive instruments, critically limiting their accessibility on the factory floor [16]. Their time-consuming nature significantly delays decision-making in production, leading to undesirable outcomes like deteriorated quality of products and machine maintenance [16, 17].

Spatial interpolation, which produces estimations at unmeasured locations based on observed neighboring ones, can generate a denser dataset from coarser and less expensive measurements [4, 16]. Conventional non-statistical methods, such as nearest neighbor, linear and cubic interpolation [18, 19], provide limited precision as they do not adapt to specific data or problem characteristics. In the field of spatial statistics [20], various methods based on stochastic processes have been developed to leverage data-specific statistical correlations for spatial interpolation. Among these, kriging-type methods are predominantly used due to their simplicity and generally satisfactory performance [16]. They are also known as Gaussian process regression in statistical and machine learning communities [21], since they are equivalent to modeling and inference using a Gaussian process. Such processes capture statistical correlation through covariance functions, which need to be properly modeled with measurement data. When applying Gaussian process regression, it is typically required that the covariance model is stationary and either isotropic or, at most, geometrically

anisotropic [20].

Periodic spatial patterns exist in many disciplines, such as materials science [22], ecology [23], and remote sensing [24]. Periodicity is also common in manufactured surfaces. Often, periodic textures are inadvertent byproducts of manufacturing processes such as machining [3, 25–27], additive manufacturing [11, 28], and woven surface fabrication [29]. Additionally, repetitive structures or patterns can be manufactured over surfaces using techniques including machining [30], micro-/nano-machining [31–33], additive manufacturing methods such as TPL [9, 10, 34], molding [35, 36], and various laser surface modification technologies [35, 37–42]. Such structural surfaces are frequently engineered to fulfill specific functions [40]. For example, optical elements such as blazed gratings [32] and micro-lens arrays [33] are designed for light manipulation. Other functional surfaces include laser-processed superhydrophobic [41] and antireflective/superwicking surfaces [43], as well as textured tool surfaces for UMW [44], cutting [42], and molding [35].

However, the assumption of isotropic correlations can be hardly satisfied when modeling periodic surfaces. While maintaining the stationarity assumption, the covariance function is expected to exhibit a discernible periodic pattern due to the inherent periodicity of the surface. Such a pattern is incompatible with isotropy for any nontrivial case in a two-dimensional space, making isotropic models oversimplified and highly inaccurate for capturing such complexities. Maculotti et al. [28] provided an illustrative example. It is possible to model such correlation structures by adopting flexible nonparametric methods and/or combining proper covariance functions [45] to account for both periodicity and the induced anisotropy. Nevertheless, such an uncommon model must be carefully crafted, and is often more computationally expensive to fit because of a much higher degree of freedom.

Furthermore, numerical issues may exist with periodic correlation even if it is properly modeled. On a periodic surface, the value at a location may correlate strongly with some distant observations. It is possible that strong long-range correlations result in dense and potentially ill-conditioned matrices at the stage

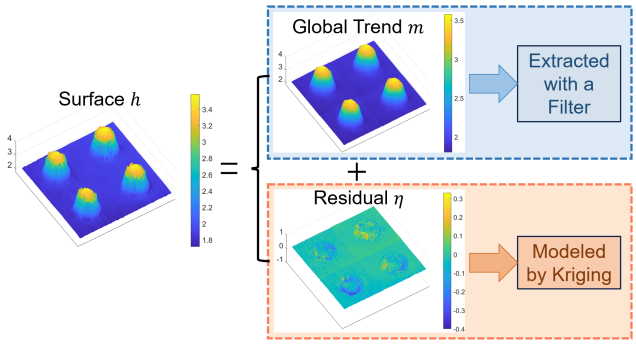

Figure 1: Overview of the FK framework.

of inference, thus leading to poor scalability and numerical singularities [46].

One approach to circumvent these complications is to separate the difficult-to-model periodic component using an alternative method, and the residual with simpler structure becomes easier to treat. Inspired by band-limited filters in signal processing, we propose to estimate the periodic part with a spatial version of such filters. Then, the residual can be captured more adequately by conventional isotropic models with significantly reduced correlation range, and interpolation can be performed effectively using simple kriging. We name this procedure as filtered kriging (FK). Figure 1 illustrates the FK framework. FK bypasses the dilemma of having to address a complex and atypical model prone to numerical issues, or suffering from lack of fit and compromised interpolation accuracy. Thus, the FK strategy effectively enhances kriging-type methods on surfaces with periodic patterns. Periodic surfaces from two real-world manufacturing applications including TPL and UMW are used to illustrate the proposed FK method and demonstrate its effectiveness.

The remainder of this paper is organized as follows. Section 2 provides preliminaries and a detailed description of the FK procedure. In Section 3, the formulation of FK procedures is further explained and analyzed using frequency domain techniques and insights from signal processing. These analyses lead to conditions under which FK to be effective. Subsequently, a practical bandpass filter design strategy for periodic surfaces is discussed in Section 4. Section 5

presents two case studies. Finally, Section 6 concludes the paper.

2. The FK Method

2.1. Preliminaries and notations

Let the value (e.g., height) of interest be a function h over a spatial region $D \subset \mathbb{R}^d$ ($d = 2$ for surface problems). The function is measured at N locations $\mathbf{x}_1, \mathbf{x}_2, \ldots, \mathbf{x}_N \in D$, which are aggregated into an $N \times d$ matrix $\mathbf{X}$ with the j-th row being $\mathbf{x}_j^\top$. Throughout this paper, boldface lowercase letters are used to represent vectors of exactly d dimensions. Measurements are organized into a column vector $H = h(\mathbf{X}) = (h_1, h_2, \ldots, h_N)^\top$, where $h_j = h(\mathbf{x}_j)$. Note that the measurement error is ignored for simplicity, and will be treated in Section **??** of the Supplementary Information (SI). An interpolation method I yields a function $I(H) = h_{\text{Int}} : D \to \mathbb{R}$ given the measurements [16]. In other words, for $\mathbf{x}_0 \in D$, it produces an estimation $h_{\text{Int}}(\mathbf{x}_0)$ of $h(\mathbf{x}_0)$ given H and $\mathbf{X}$.

Spatial statistical methods model the function as a realization of a continuously indexed spatial stochastic process $h = \{h(\mathbf{x}) : \mathbf{x} \in D\}$, and statistical inference methods are used to produce the estimation. Since this work focuses on kriging-type methods, we assume $h \sim GP(0, c)$ is a stationary zero-mean Gaussian process on $D \subset \mathbb{R}^d$ with covariance function $c(\mathbf{x}, \mathbf{x}') = c(\mathbf{x} - \mathbf{x}')$. Then, for interpolation simple kriging yields the best linear unbiased prediction $\hat{h}(\mathbf{x}_0)$ of $h(\mathbf{x}_0)$ given H:

$$\hat{h}(\mathbf{x}_0) = c(\mathbf{x}_0, \mathbf{X})\mathbf{C}^{-1}H, \tag{1}$$

where $c(\mathbf{x}_0, \mathbf{X})$ denotes the $1 \times N$ matrix of the covariances evaluated at all pairs of points in $\mathbf{x}_0$ and $\mathbf{X}$, and similarly for $\mathbf{C} = c(\mathbf{X}, \mathbf{X})$. By relaxing the assumption about the mean function of a Gaussian process, major kriging variants such as ordinary kriging and kriging with external drift (KED) can be obtained.

A function or signal is composed of trigonometric components with different frequencies in the view of Fourier analysis, and filters can be used to change the amplitudes of these frequency components. A bandpass filter preserves components within a certain frequency range and attenuates those outside that

range. Thus, it can be used to extract components of certain periods from a function. Similar procedures can be applied to stochastic processes.

The following notations are used for Fourier analysis of deterministic functions. The spectrum $\widetilde{f}(\boldsymbol{\xi})$ of a function $f(\mathbf{x})$ on $\mathbb{R}^d$ is defined as

$$\widetilde{f}(\boldsymbol{\xi}) = \int e^{-2\pi i \langle \boldsymbol{\xi}, \mathbf{x} \rangle} f(\mathbf{x}) d\mathbf{x}. \tag{2}$$

Under mild assumptions we have

$$f(\mathbf{x}) = \int e^{2\pi i \langle \mathbf{x}, \boldsymbol{\xi} \rangle} \widetilde{f}(\boldsymbol{\xi}) d\boldsymbol{\xi}. \tag{3}$$

A function f on $\mathbb{R}^d$ is said to be periodic, if there exists d non-collinear vectors $\mathbf{p}_1, \mathbf{p}_2, \ldots, \mathbf{p}_d$, such that

$$f(\mathbf{x}) = f(\mathbf{x} - \mathbf{p}_1) = f(\mathbf{x} - \mathbf{p}_2) = \cdots = f(\mathbf{x} - \mathbf{p}_d). \tag{4}$$

The matrix $\mathbf{P} = (\mathbf{p}_1, \mathbf{p}_2, \ldots, \mathbf{p}_d)$ is referred to as the periodicity matrix [47].

2.2. Description of the FK procedure

The FK procedure contains the following four steps:

Step 1 **Preparations.** First, the surface h is measured at locations $\mathbf{X}$ to obtain spatial data $H = h(\mathbf{X})$. Based on sampled data and/or existing process knowledge, the periodicity matrix $\mathbf{P}$ of the pattern is determined. Then, a linear bandpass filter F is designed to center its pass-bands approximately around the integer multiples of frequencies in $\mathbf{Q} = \mathbf{P}^{-1}$. The residual $h - F(h)$ after filtering (if computable) is expected to be scarcely periodic. A straightforward method to specify a discrete convolutional filter will be discussed in Section 4.

Step 2 **Pre-filtering.** Since $F(h)$ is generally not computable with only $H = h(\mathbf{X})$, an additional pre-interpolation step is introduced before applying the filter. The samples $H = h(\mathbf{X})$ are first interpolated with a simple interpolation method I, e.g., linear or cubic interpolation; the result is a function $h_{\mathrm{Int}} = I(H) : D \to \mathbb{R}$. Since the value of h_{Int} can be evaluated at any location

in the continuous interpolation region D, $h_F = F(h_{\text{Int}})$ becomes computable in D. It is expected that the periodic component could be well-preserved by the interpolation method selected, i.e., $h_F = F(h_{\text{Int}}) \approx F(h)$.

Step 3 **Kriging the residual.** The residual of pre-filtering is computed over the sampled locations: $H_{\text{res}} = H - h_F(\mathbf{X})$. Then, a stationary process h_r is used to model the residual, i.e., let observations of h_r be $h_r(\mathbf{X}) = H_{\text{res}}$. In this work, we follow the commonly used approach for model selection: fitting a parametric covariance function model via weighted least squares to the empirical covariance computed from H_{res}. Alternative approaches, e.g., likelihood-based methods [20], could also be adopted to yield a valid parametric covariance model. An estimation $\hat{h}_r$ of h_r is obtained by performing kriging with the fitted model and data H_{res}.

Step 4 **Obtaining the final estimation.** $\hat{h} = h_F + \hat{h}_r$ is used as the final estimation of h.

The FK method can be extended to account for measurement noise. Corresponding FK procedures and conditions that control the estimation error are presented in Section **??** of the SI. Symbols and notations that are frequently used are summarized in Table 1.

3. Theoretical Analysis of the FK Procedure

In this section, we first explain the formulation of FK and establish an analytical framework. Then, quantitative and qualitative assessments of FK are conducted in the case of uniform sampling over an infinite grid, where conditions allow straightforward analysis of sampling, interpolation and filtering in the frequency domain. These analyses identify conditions under which FK is effective and provide guidance for filter design. Finally, we introduce a new theorem that establishes the equivalence between kriging and cardinal series interpolation for band-limited processes, both method yielding perfect estimations in the mean square sense. With this theorem, it is proven that FK achieves identical optimal results under appropriate conditions.

Table 1: List of frequently used symbols and notations

Symbol / Notation	Description
$\mathbf{x}, \boldsymbol{\xi}, \mathbf{l} \dots$	$d \times 1$ column vectors (boldface lowercase letters)
D	d-dimensional spatial region of interest in $\mathbb{R}^d$
h	Quantity (e.g., height) over region D to be interpolated
$\mathbf{x}_1, \mathbf{x}_2, \dots, \mathbf{x}_N$	Measured locations in D
$\mathbf{X}$	$N \times d$ matrix of measured locations $\mathbf{X} = (\mathbf{x}_1, \mathbf{x}_2, \dots, \mathbf{x}_N)^\top$
$H = h(\mathbf{X})$	$N \times 1$ vector of measurements $H = (h(\mathbf{x}_1), h(\mathbf{x}_2), \dots, h(\mathbf{x}_N))^\top$
$\mathbf{P}$	Periodicity matrix defined by Eq. (4)
$h_{\text{Int}} = I(H)$	Result of pre-interpolating samples $H = h(\mathbf{X})$ with I
$h_F = F(h_{\text{Int}})$	Result of filtering h_{Int} with the filter F
$h_{\text{res}} = h - h_F$	Residual after pre-filtering
h_r	Stationary process that models the residual h_{res}
$\hat{h}, \hat{h}_r$	Estimations of h, h_r
c, c_r	Covariance functions of stochastic processes
k_{Int}, k_F, k	Convolution kernels corresponding to I, F and $F \circ I$
$\widetilde{f}(\boldsymbol{\xi}), \widetilde{k}(\boldsymbol{\xi}), \dots$	Fourier transform of function $f(\mathbf{x}), k(\mathbf{x})$, etc.

3.1. Formulation of FK and an analytical framework

As described in Section 1, challenging periodic components in h can significantly impact the performance of kriging. If h is a known deterministic function, it is well-established that such a component can be isolated using a convolutional bandpass filter F with kernel k, and this filter can be readily designed in the frequency domain. By the convolutional theorem in classical Fourier analysis, the filtered result $F(h) = h * k$ transforms to

$$\widetilde{F(h)} = \widetilde{h * k} = \widetilde{h} \cdot \widetilde{k}. \tag{5}$$

To isolate certain components, such as those related to strong periodicity, supported on a set $A \subset \mathbb{R}^d$ in the frequency domain, it suffices to designate A as the passband of the filter F. Specifically, set $\widetilde{k}(\boldsymbol{\xi}) \approx 1$ for $\boldsymbol{\xi} \in A$ and $\widetilde{k}(\boldsymbol{\xi}) \approx 0$ elsewhere. Consequently, the corresponding components within A can be effectively removed in the residual $h - F(h)$, with $\widetilde{h} - \widetilde{F(h)} = \widetilde{h} \cdot (1 - \widetilde{k}) \approx 0$ on A.

For stochastic processes, Fourier analysis can be performed in a similar way as the deterministic case. Following the spectral representation theorem [48], a mean square continuous stationary Gaussian process $h \sim GP(0, c)$ can be represented as

$$h(\mathbf{x}) = \int e^{2\pi i \langle \mathbf{x}, \boldsymbol{\xi} \rangle} R(d\boldsymbol{\xi}), \tag{6}$$

where R is a random measure [48] called the spectral process corresponding to h. It is often assumed that R can be written as $R(d\boldsymbol{\xi}) = \rho(\boldsymbol{\xi}) Z(d\boldsymbol{\xi})$, where $\rho(\boldsymbol{\xi})$ is a square-integrable function, and Z is a Gaussian white noise based on Lebesgue measure in $\mathbb{R}^d$. The term ρ (or $R(d\boldsymbol{\xi}) = \rho(\boldsymbol{\xi}) Z(d\boldsymbol{\xi})$) resembles the behavior of $\widetilde{h}$ (or $\widetilde{h}(\boldsymbol{\xi}) d\boldsymbol{\xi}$) in the deterministic case. The covariance function is

$$c(\mathbf{x}, \mathbf{x}') = \int e^{2\pi i \langle \mathbf{x} - \mathbf{x}', \boldsymbol{\xi} \rangle} \mathbb{E}[|R(d\boldsymbol{\xi})|^2] = \int e^{2\pi i \langle \mathbf{x} - \mathbf{x}', \boldsymbol{\xi} \rangle} |\rho(\boldsymbol{\xi})|^2 d\boldsymbol{\xi}, \tag{7}$$

where $|\rho|^2$ is called the spectral density of h.

With preceding definitions, convolutional filtering operates on a stochastic process h in a similar manner

$$\begin{aligned} (F(h))(\mathbf{x}) = \widetilde{(h * k)}(\mathbf{x}) &= \int e^{2\pi i \langle \mathbf{x} - \mathbf{x}', \boldsymbol{\xi} \rangle} \rho(\boldsymbol{\xi}) Z(d\boldsymbol{\xi})\, k(\mathbf{x}') d\mathbf{x}' \\ &= \int e^{2\pi i \langle \mathbf{x}, \boldsymbol{\xi} \rangle}\, (\rho \cdot \widetilde{k})(\boldsymbol{\xi})\, Z(d\boldsymbol{\xi}), \end{aligned} \tag{8}$$

and isolates components with strong periodic correlation given a proper band-pass filter. The residual $h - F(h)$ remains to be a stationary Gaussian process, but with periodic correlations eliminated, making it significantly easier to model than h prior to filtering.

When the process h is only partially observed over a discrete set of sample locations $\mathbf{X}$, the aforementioned convolutional filter generally becomes inapplicable. To address this case, the Step 2 of FK integrates the filter with an additional pre-interpolation step to approximate the effect of the original filter F and adapt to discrete measurements $H = h(\mathbf{X})$. Specifically, a substitute $h_{\text{Int}} = I(H)$ is constructed for h with the pre-interpolation I. Then, $h_F = F(h_{\text{Int}})$ is computed as a surrogate for $F(h)$. Given a properly designed filter F in Step 1 of FK, the residual $h_{\text{res}} = h - h_F \approx h - F(h)$ can be properly modeled and estimated from $h_{\text{res}}(\mathbf{X})$ using kriging in Step 3.

Up to now, the FK procedure has been formulated through an attempt to approximate bandpass filtering of a stationary stochastic process. From this perspective, when selecting the pre-interpolation method, it is desired that h_{Int} approximates h accurately especially within the filter's passbands. FK makes improvements based on the pre-interpolation result by replacing its components outside the passbands with more accurate kriging estimations. This approach also implies that the filter should have as narrow a bandwidth as possible, provided it completely isolates the difficult-to-model components, to minimize the passage of errors from pre-interpolation into the final result. These intuitive conclusions will be further substantiated by analyses in subsequent sections.

Although above formulation of FK does not rely on a specific sampling strategy or pre-interpolation method, for the purpose of quantitative characterization, sampling over a uniform, infinite grid and linear pre-interpolation with respect to $h(\mathbf{X})$ are assumed throughout the subsequent analysis. Without loss of generality, samples are further assumed to be taken over the infinite integer grid $\mathbb{Z}^d$, which can always be achieved through some linear transformation. Infinite grid assumption leads to neater derivation and conclusions, which might be regarded as the increasing-domain asymptotics for samples in a finite region (as discussed in Section **??** of the SI). Some empirical comments are also made in Section **??** of the SI for general sampling and pre-interpolation methods.

3.2. A quantitative analysis of FK procedures

Under the analytical framework outlined in Section 3.1, FK procedures are analyzed to derive an upper bound for the discrepancy between FK and the theoretically optimal Gaussian process regression. This analysis reveals the condition under which FK approaches near-optimal performance.

First, the procedure of uniform sampling is formulated as the product with a Dirac comb:

$$h_s(\mathbf{x}) = h(\mathbf{x}) \cdot \sum_{\mathbf{n}\in\mathbb{Z}^d} \delta(\mathbf{x}-\mathbf{n}) \tag{9}$$

After sampling, interpolating the data $h(\mathbf{X})$ linearly is equivalent to convolution

with an interpolation kernel k_{Int} [18]:

$$h_{\text{Int}} = h_s * k_{\text{Int}}. \tag{10}$$

Filtering the interpolated data h_{Int} is also equivalent to a convolution with kernel k_F. Then, it follows from the associativity of convolution that

$$h_F = h_{\text{Int}} * k_F = h_s * (k_{\text{Int}} * k_F) = h_s * k, \tag{11}$$

where $k = k_{\text{Int}} * k_F$, whose spectrum is

$$\widetilde{k}(\boldsymbol{\xi}) = \widetilde{k_{\text{Int}}}(\boldsymbol{\xi}) \cdot \widetilde{k_F}(\boldsymbol{\xi}). \tag{12}$$

As shown in Section **??** of the SI, h_F could be written as

$$h_F(\mathbf{x}) = \int e^{2\pi i \langle \mathbf{x}, \boldsymbol{\xi} \rangle} \widetilde{K}(\boldsymbol{\xi}; \mathbf{x}) R(d\boldsymbol{\xi}), \tag{13}$$

where $\widetilde{K}(\boldsymbol{\xi}; \mathbf{x})$ is defined as

$$\widetilde{K}(\boldsymbol{\xi}; \mathbf{x}) = \sum_{\mathbf{l} \in \mathbb{Z}^d} e^{2\pi i \langle \mathbf{x}, \mathbf{l} \rangle} \widetilde{k}(\boldsymbol{\xi} + \mathbf{l}). \tag{14}$$

It is straightforward to verify that, although $h_{\text{res}} = h - h_F$ is not stationary by itself, it coincides with a stationary process h_r over the sampling integer grid $\mathbb{Z}^d$, which is modeled and estimated in Step 3 of FK:

$$h_r(\mathbf{x}) = \int e^{2\pi i \langle \mathbf{x}, \boldsymbol{\xi} \rangle} (1 - \widetilde{K}(\boldsymbol{\xi}; \mathbf{0})) R(d\boldsymbol{\xi}). \tag{15}$$

Because h_r is stationary, its covariance c_r over the grid can be computed from $h_r|_{\mathbb{Z}^d} = h_{\text{res}}|_{\mathbb{Z}^d} = H_{\text{res}}$ using Eq. (16). The estimator is unbiased, and the equality holds in the mean square sense whenever $c_r(\mathbf{l}) \to 0$ as $|\mathbf{l}| \to \infty$ (see Section **??** of the SI for relevant conditions and proof).

$$\begin{aligned} c_r(\mathbf{m}, \mathbf{n}) &= \mathbb{E}[h_r(\mathbf{m}) h_r(\mathbf{n})] \\ &= \lim_{M \to \infty} \frac{1}{|2M+1|^d} \sum_{\mathbf{l}=-M}^{M} h_r(\mathbf{l}+\mathbf{m}) h_r(\mathbf{l}+\mathbf{n}), \end{aligned} \tag{16}$$

where each entry of $\mathbf{l} = (l^{(1)}, \ldots, l^{(d)})$ in the sum ranges from $-M$ to M. The covariance function $c_r(\mathbf{x})$ is then estimated from its values over the grid.

The total error of FK is

$$\begin{aligned} & h - (h_F + \hat{h}_r) \\ & = (h - h_F - h_r) + (h_r - \hat{h}_r) \\ & = r_1 + r_2, \end{aligned} \tag{17}$$

where $r_1 = h_{\text{res}} - h_r$, and $r_2 = h_r - \hat{h}_r$.

The first part of the error r_1 is the difference between h_{res} and its stationary version h_r. From Eq. (13) and (15),

$$r_1(\mathbf{x}) = \int e^{2\pi i \langle \mathbf{x}, \boldsymbol{\xi} \rangle} \left(\widetilde{K}(\boldsymbol{\xi}, 0) - \widetilde{K}(\boldsymbol{\xi}, \mathbf{x}) \right) R(d\boldsymbol{\xi}), \tag{18}$$

whose variance is bounded by (see Section **??** of SI for details)

$$\mathbb{E}[|r_1(\mathbf{x})|^2] \leq 4 \int |\rho(\boldsymbol{\xi})|^2 \left(\sum_{|\mathbf{l}| \geq 1} |\widetilde{k}(\boldsymbol{\xi} + \mathbf{l})| \right)^2 d\boldsymbol{\xi}. \tag{19}$$

Convergence of $\sum_{|\mathbf{l}| \geq 1} |\widetilde{k}(\boldsymbol{\xi} + \mathbf{l})|$ could be guaranteed by sufficient smoothness property of k (usually essentially of k_{Int}). Comparing Eq. (19), (13) and (8), it can be seen that r_1 is essentially a type of aliasing error that persists or is introduced during the process of pre-interpolation and filtering, from a signal processing perspective. The integral upper bound above could then be made small given the following condition.

Condition 1: The overlap between $|\rho|^2$ and the sum $\widetilde{K}_1(\boldsymbol{\xi}) = \sum_{|\mathbf{l}| \geq 1} |\widetilde{k}(\boldsymbol{\xi} + \mathbf{l})|$ is small.

For the second part of the error $r_2 = h_r - \hat{h}_r$, if the covariance function c_r is known, then the error variance $\mathbb{E}[r_2^2]$ is minimized, because the simple kriging estimator $\hat{h}_r$ is already the minimum mean square error estimation of h_r. The estimator $\hat{h}_r$ could deviate from the optimum only because of error in the estimated covariance function. Under conditions stated in Section **??** of the SI, values of c_r over the integer grid could be estimated correctly with Eq. (16), and off-grid values can be further obtained through interpolation. The estimation error may be controlled with extra conditions like Lipschitz

continuity, and could be eliminated if a stronger band-limitation assumption is imposed (see Section 3.4).

3.3. Effect of bandpass filtering

In this section, we perform a qualitative analysis of the bandpass filtering procedure in FK, explaining how it enhances conventional covariance models and deriving criteria for filter design accordingly. To illustrate this, consider the typical decomposition of the process h into a global trend m and local spatial variation η:

$$h(\mathbf{x}) = m(\mathbf{x}) + \eta(\mathbf{x}), \tag{20}$$

where m and η are independent zero-mean stationary Gaussian processes. For surfaces with periodic patterns, the term m is supposed to account for the strong periodic trend, while in general, we may assume η can be readily fitted by conventional models (e.g., isotropic ones adopted in the case studies of this paper).

To characterize m and η in the frequency domain, let their spectral process be $p(\boldsymbol{\xi})V(d\boldsymbol{\xi})$ and $q(\boldsymbol{\xi})W(d\boldsymbol{\xi})$, respectively, where p and q are square-integrable functions, and V and W are independent Gaussian white noise in $\mathbb{R}^d$. Because m captures the strong periodicity, its spectral density $|p|^2$ is concentrated around a few integer linear combinations of columns in $\mathbf{P}^{-1}$. In contrast, q tends to distribute more uniformly across the frequency domain, with η representing smaller-scale variation. Both p and q exhibit rapid decay when the process h is adequately sampled.

With these notations, the filtered h_F is composed of two parts:

$$h_F = \left((m+\eta) \cdot \sum_{\mathbf{n}\in\mathbb{Z}^d} \delta(\cdot - \mathbf{n}) \right) * k = m_F + \eta_F. \tag{21}$$

Similar to Eq. (13), $m_F(\mathbf{x}) = \int e^{2\pi i\langle \cdot, \boldsymbol{\xi}\rangle} p(\boldsymbol{\xi}) \widetilde{K}(\boldsymbol{\xi}; \mathbf{x}) V(d\boldsymbol{\xi})$, which can be further decomposed into

$$m_F(\mathbf{x}) = \int e^{2\pi i\langle \mathbf{x}, \boldsymbol{\xi}\rangle} p(\boldsymbol{\xi}) \widetilde{k}(\boldsymbol{\xi}) V(d\boldsymbol{\xi}) + \int e^{2\pi i\langle \mathbf{x}, \boldsymbol{\xi}\rangle} p(\boldsymbol{\xi}) \widetilde{K}_r(\boldsymbol{\xi}; \mathbf{x}) V(d\boldsymbol{\xi}), \tag{22}$$

where

$$\widetilde{K}_r(\boldsymbol{\xi};\mathbf{x}) = \widetilde{K}(\boldsymbol{\xi};\mathbf{x}) - \widetilde{k}(\boldsymbol{\xi}) = \sum_{\mathbf{l}\in\mathbb{Z}^d,\mathbf{l}\neq\mathbf{0}} e^{2\pi i\langle\mathbf{x},\mathbf{l}\rangle}\widetilde{k}(\boldsymbol{\xi}+\mathbf{l}). \tag{23}$$

It is evident that first term of Eq. (22) corresponds to the "pure" filtering effect as seen in Eq. (8), while the latter term indicates how much pre-filtering is affected by the aliasing effect due to sampling. We may expect that $p\widetilde{k} \approx p$, which suggests that the first term closely approximates m, provided the filter's passbands are designed to cover frequencies where p's energy concentrates. Additionally, if $\widetilde{k}$ and p decay rapidly, the overlap between p and $\widetilde{K}_r$ will be minimal, indicating a low variance in the aliasing term.

The second part

$$\eta_F(\mathbf{x}) = \int e^{2\pi i\langle\mathbf{x},\boldsymbol{\xi}\rangle} q(\boldsymbol{\xi})\widetilde{K}(\boldsymbol{\xi};\mathbf{x})W(d\boldsymbol{\xi}) \tag{24}$$

will be minimal if the overlap between $|q|^2$ and $\widetilde{K}$ is small. Consequently, when the total passband of $\widetilde{k}$ is narrow, η_F becomes negligible, given the existing assumptions about q.

In summary, the analysis above shows that FK approximates the typical decomposition of spatial processes into a global trend and a local variation: $h_F = m_F + \eta_F \approx m$, when the filter is intentionally designed to pass the strong periodic global trend m while suppressing local variation η, and when the process is adequately sampled. In other words, bandpass pre-filtering could separate out the periodic m, such that the residual $h_{\text{res}} = (m+\eta) - h_F \approx \eta$ can be modeled more easily using conventional methods. As a result, the following design criterion is established for the filter corresponding to $\widetilde{k}$:

Condition 2: $m - m_F$ is sufficiently suppressed, while the filter has a narrow total bandwidth.

3.4. Kriging for band-limited processes and Shannon sampling theorem

From analyses in the previous two sections, it is evident that FK is influenced by aliasing error. In this section, through a novel theorem, we demonstrate that when a band-limited process is sampled without aliasing, FK is also free from

aliasing error and consequently yields optimal estimations under appropriate conditions.

According to the classical Nyquist-Shannon sampling theorem, a band-limited deterministic function can be fully recovered from its samples over the integer grid using the cardinal series [47]. Here a deterministic function y is said to be band-limited, if its Fourier transform $\widetilde{y}$ satisfies $\widetilde{y} = \widetilde{y} \cdot \mathrm{rect}$, where the rect function in d-dimensional space is defined from standard 1-D rectangular function as $\mathrm{rect}(\boldsymbol{\xi}) \coloneqq \prod_{j=1}^{d} \mathrm{rect}(\xi^{(j)})$ for $\boldsymbol{\xi} = (\xi^{(1)}, \ldots, \xi^{(d)})$. Similar definitions and theorem hold for stationary stochastic processes, as shown in [47, Sec. 3.5]:

Lemma 1. *A zero-mean wide sense stationary process $y(\mathbf{x})$ is said to be band-limited, if it has spectral density s.t.*

$$\widetilde{c}(\boldsymbol{\xi}) = \widetilde{c}(\boldsymbol{\xi})\mathrm{rect}(\boldsymbol{\xi}), \tag{25}$$

i.e., its covariance function c is band-limited.

The cardinal series $\hat{y}^{\mathrm{Card}}$ for y converges in the mean square sense. Specifically, define

$$\hat{y}^{\mathrm{Card}}(\mathbf{x}) = \sum_{\mathbf{n} \in \mathbb{Z}} y(\mathbf{n})\mathrm{sinc}(\mathbf{x} - \mathbf{n}), \tag{26}$$

where

$$\mathrm{sinc}(\mathbf{x}) \coloneqq \prod_{j=1}^{d} \mathrm{sinc}(x^{(j)}) = \prod_{j=1}^{d} \frac{\sin(\pi x^{(j)})}{\pi x^{(j)}}, \tag{27}$$

for $\mathbf{x} = (x^{(1)}, \ldots, x^{(d)})$.

Then $\hat{y}^{\mathrm{Card}}(\mathbf{x})$ equals to $y(\mathbf{x})$ in the mean square sense:

$$\mathbb{E}\left[(\hat{y}^{\mathrm{Card}}(\mathbf{x}) - y(\mathbf{x}))^2\right] = 0. \tag{28}$$

In the Gaussian process case where a spectral density exists, h is band-limited if $|\rho(\boldsymbol{\xi})|^2 = |\rho(\boldsymbol{\xi})|^2 \cdot \mathrm{rect}(\boldsymbol{\xi})$ (or equivalently, $R(d\boldsymbol{\xi}) = R(d\boldsymbol{\xi}) \cdot \mathrm{rect}(\boldsymbol{\xi})$). Practically, the band-limitation assumption has the following implications.

- Samples on the integer grid are sufficient for capturing all surface variations, i.e., sampling is free from aliasing.
- Since almost every sample path of a band-limited process is smooth, i.e., infinitely differentiable [49], it implies that the surface is smooth and measurement noise is ignored.

In the ideal case where h is a band-limited process, we are able to obtain a perfect estimation in the mean square sense from samples according to Lemma 1. Moreover, the simple kriging estimator is also perfect in this case, as stated in the following new theorem.

Theorem 1. *Given observations of a band-limited process $y(\mathbf{x})$ over a finite regular grid that is sufficiently dense for sampling without aliasing, the best linear unbiased predictor converges to corresponding cardinal series in the mean square sense, as the size of the grid tends to infinity, as long as the covariance function c is strictly positive definite (such that the best linear unbiased predictor exists).*

Without loss of generality, let $\mathbf{X} = \mathbf{X}_N$ contain all integer points in $[-N, N]^d$, $Y = Y_N = y(\mathbf{X}_N)$, and let the spectral support of y be contained in $[-1/2, 1/2]^d$. In this case, the best linear unbiased predictor $\hat{y}_N(\mathbf{x}) = c(\mathbf{x}, \mathbf{X})c(\mathbf{X}, \mathbf{X})^{-1}Y$ tends to $y(\mathbf{x})$ in the mean square sense as $N \to \infty$.

Particularly, the best linear unbiased predictor $\hat{y}_N$ and the partial sum of the cardinal series $\hat{y}^{\mathrm{Card}}$ yields the same limit y when the process covariance is band-limited and strictly positive definite.

Proof. See Section **??** of the SI for proof and relevant remarks. □

Perfect reconstruction can be achieved by the FK procedure in this ideal case, given some additional conditions, and specifying the pre-filtering to be band-limited: $\widetilde{k}(\boldsymbol{\xi}) = \widetilde{k}(\boldsymbol{\xi}) \cdot \mathrm{rect}(\boldsymbol{\xi})$. See discussions in Section **??** of the SI for details.

4. Design and Implementation of the FK Pre-filter

4.1. General requirements for FK filters

Following the analysis in Section 3.2, **Condition 1** should be approached through k. Additionally, **Condition 2** is required to ensure the residual after filtering can be more readily modeled with common models.

Following Eq. (13) and (21),

$$(m - m_F)(\mathbf{x}) = \int e^{2\pi i \langle \mathbf{x}, \boldsymbol{\xi} \rangle} p(\boldsymbol{\xi}) \left((1 - \widetilde{k}(\boldsymbol{\xi})) - \widetilde{K}_r(\boldsymbol{\xi}; \mathbf{x}) \right) V(d\boldsymbol{\xi}). \tag{29}$$

The term $p\widetilde{K}_r$ is already suppressed if **Condition 1** is satisfied. Thus, **Condition 2** could be rephrased as

Condition 2': $p(1-\widetilde{k})$ is sufficiently suppressed, i.e., filtering passes the periodic component thoroughly. Meanwhile, $\widetilde{k}$ has a narrow total bandwidth.

Since most interpolation methods resemble the behavior of some low-pass filter, we may assume $\widetilde{k_{\mathrm{Int}}} \approx \mathrm{rect}(\cdot)$, and **Conditions 1,2'** for $\widetilde{k}$ ($\approx \mathrm{rect} \cdot \widetilde{k_F}$) can be further decoupled for simplification into:

(a) The pre-interpolation (k_{Int}) has a passband which covers that of m, and its frequency response decays rapidly outside this passband.

(b) The filter (k_F) maintains approximately unit gain within its passbands, which are narrow yet cover regions where m's energy is concentrated.

4.2. Design of a discrete bandpass filter

In practice, interpolation values are usually inquired over a regular grid denser than measurements. In such cases, it is convenient to use convolutional discrete filters.

Let the periodicity matrix be $\mathbf{P} = (\mathbf{p}_1, \ldots, \mathbf{p}_d)$. We may use a filter of the form

$$k_F(\mathbf{x}) = \sum_{\mathbf{m}\in\mathbb{Z}^d} w_{\mathbf{m}} \delta(\mathbf{x} - \mathbf{P}\cdot\mathbf{m}), \tag{30}$$

where only finite terms of $w_{\mathbf{m}}$ are nonzero. It simplifies design and analysis to use $w_{\mathbf{m}} = w(\mathbf{P}\cdot\mathbf{m})$ for some compactly supported function w. In this case,

$$k_F(\mathbf{x}) = w(\mathbf{x}) \cdot \left(\sum_{\mathbf{m}\in\mathbb{Z}^d} \delta(\mathbf{x} - \mathbf{P}\cdot\mathbf{m}) \right). \tag{31}$$

Considering that the Fourier transform of $\sum_{\mathbf{m}\in\mathbb{Z}^d} \delta(\mathbf{x} - \mathbf{P}\cdot\mathbf{m})$ is [47]

$$|\det \mathbf{Q}| \sum_{\mathbf{m}\in\mathbb{Z}^d} \delta(\boldsymbol{\nu} - \mathbf{Q}\cdot\mathbf{m}), \tag{32}$$

where $\mathbf{Q} = \mathbf{P}^{-1}$, the frequency response of such filter $\widetilde{k_F}$ is

$$\widetilde{k_F} = \widetilde{w} * |\det \mathbf{Q}| \sum_{\mathbf{m}\in\mathbb{Z}^d} \delta(\cdot - \mathbf{Q}\cdot\mathbf{m}) = |\det \mathbf{Q}| \sum_{\mathbf{m}\in\mathbb{Z}^d} \widetilde{w}(\cdot - \mathbf{Q}\cdot\mathbf{m}). \tag{33}$$

Note that $\widetilde{k_F}$ is periodic. By defining $\widetilde{w}$ as a lowpass filter with a narrow passband, a bandpass filter is obtained, with same passbands of $\widetilde{w}$ centered at integer multiples of fundamental frequencies $\mathbf{Q}$.

To ensure the bandpass filter $\widetilde{k_F}$ achieves unit gain at $\mathbf{Q}\mathbb{Z}^d = \{\mathbf{Q}\cdot\mathbf{m}\,|\,\mathbf{m}\in\mathbb{Z}^d\}$, according to Eq. (33), the amplitude of w may be adjusted so that $\widetilde{w}(\mathbf{0}) = |\det\mathbf{P}|$ if $\widetilde{w}$ decays rapidly. Alternatively, exact unit gain can be achieved by setting

$$\sum_{\mathbf{m}\in\mathbb{Z}^d} w_{\mathbf{m}} = 1. \tag{34}$$

Since the passband of $\widetilde{w}$ is replicated at intervals of $\mathbf{Q}$ in $\widetilde{k_F}$, it is necessary to ensure this passband is containd within the frame spanned by columns of Q and has significantly smaller volume compared with $|\det\mathbf{Q}|$. Practically, this often requires w to have a spatial bandwidth extending over more than three periods in each direction. There is a trade-off in determining the width of w: a wider w yields narrower passbands, which makes it less prone to aliasing error, but it also increases the risk of not completely isolating the periodic trend.

Usually, w decays monotonically as the distance increases. When w assigns equal weights, FK resembles the "seasonal adjustment" technique for time series analysis [50].

Filters may be combined to form a new filter with passband being the union of individual ones. For example, the passbands of two filters F_1 and F_2 can be merged by taking

$$F = F_1 + F_2\circ(\mathrm{id} - F_1) = F_1 + F_2 - F_2\circ F_1, \tag{35}$$

where id is the identity mapping and $\circ$ represents the composition of mappings.

4.3. Practical considerations for implementation

We make the following two remarks regarding the implementation of the filter.

First, computational efficiency can be improved for filtering by adaptation to the interpolation grid, which reduces the discrete filter to a conventional digital filter. Let the pre-interpolation be conducted over the grid $\mathbf{L}_0\mathbb{Z}^d$, i.e., $h_{\mathrm{Int}}(\mathbf{L}_0\cdot\mathbf{n})$ is obtained for $\mathbf{n}\in\mathbb{Z}^d$ in the pre-interpolation step. Applying

previous bandpass filter to h_{Int} results in

$$h_F(\mathbf{x}) = (h_{\text{Int}} * k_F)(\mathbf{x}) = \sum_{\mathbf{m}\in\mathbb{Z}^d} w_{\mathbf{m}} \cdot h_{\text{Int}}(\mathbf{x} - \mathbf{P}\cdot\mathbf{m}). \tag{36}$$

If further $\mathbf{L}_0^{-1}\mathbf{P}$ is an integer matrix, for $\mathbf{x} = \mathbf{L}_0 \cdot \mathbf{n}$ on the grid, then

$$h_F(\mathbf{L}_0 \cdot \mathbf{n}) = \sum_{\mathbf{m}\in\mathbb{Z}^d} w_{\mathbf{m}} \cdot h_{\text{Int}}(\mathbf{L}_0 \cdot (\mathbf{n} - \mathbf{L}_0^{-1}\mathbf{P}\cdot\mathbf{m})), \tag{37}$$

which only involves on-grid values in the computation, making the number of pre-interpolation inquiries independent of the filter size. When $\mathbf{L}_0^{-1}\mathbf{P}$ is not integer, the rounded value $[\mathbf{L}_0^{-1}\mathbf{P}\cdot\mathbf{m}]$ may be used as an approximation to avoid off-grid evaluations.

Second, in practice measurements can only be made over a finite domain. Consequently, filter evaluation always has to deal with missing values as it approaches to boundaries. One common method to address this issue is padding. Alternatively, Eq. (34) suggests a simple way to modify the filter weights if there are terms unavailable (e.g., exceeding the boundaries) for computing the full filter: rescaling remaining weights for available terms such that they sum up to be one. For the aforementioned bandpass filter design, this adjustment strategy keeps the peaks in passbands unchanged. See Section **??** of the SI for details.

5. Case Studies

In this section, we demonstrate the effectiveness of FK with two case studies that examine TPL-manufactured hemisphere structures [9, 10] and UMW tool surfaces with pyramid-shaped knurls [17, 45], respectively. Both case studies involve periodic surfaces, for which common ordinary kriging with isotropic covariance is demonstrated inapplicable.

High-resolution surface data in the form of regular grid are collected with a 3D microscope in both case studies. Information about the two datasets are summarized in Table 2. Then, downsampling is used to simulate data obtained from a measurement system of lower resolution. The true data serves as the

Table 2: Summary of datasets for case studies.

Case study No.	1	2
Surface name	TPL surfaces [9, 10]	UMW tool surfaces [17, 45]
Descriptions	Surface manufactured by a Nanoscribe Photonic Professional GT 3D printer	Anvil tool surfaces from a Brandson UMW machine
Periodic pattern	5×5 hemisphere structures	Repetitive pyramid-shaped knurls
Approximate periodicity matrix	$\begin{pmatrix} 7.5\mu\text{m} & 0 \\ 0 & 7.5\mu\text{m} \end{pmatrix}$	$1.436\text{mm} \cdot \begin{pmatrix} 1/2 & 1/2 \\ -1/2 & 1/2 \end{pmatrix}$
Measurement instrument	Keyence VK-X1000 confocal laser microscope	Keyence VK-9700 confocal laser microscope
Measurement resolution	94.8nm/pixel	22.032µm/pixel
Number of surfaces in the dataset	5	6
Size of measurement data	406×400	163×900

ground truth and root-mean-squared errors (RMSEs) are computed to evaluate the performance of candidate interpolation methods. Specifically, the data is uniformly downsampled with a step of three in both vertical and horizontal directions. Thus, one out of nine locations in each 3×3 grid is kept as a measured point, which still form a regular grid. The same ground truth data is sampled nine times with different starting locations to evaluate how much the result could be affected by uncertainties in the sampling step.

FK is compared with three state-of-the-art interpolation techniques: (1) bilinear spline, (2) bicubic spline, and (3) KED. KED is a common yet sufficiently general variant of kriging. It models the large-scale trend (m) as a linear combination of multiple basis functions, and the rest variation (η) as a zero-mean Gaussian process. As special cases, KED is termed ordinary or simple kriging, when the unknown mean is assumed to be constant or zero. Although ordinary kriging was performed for the same dataset in [45], and is more standard than the KED adopted here, it is not included in the comparison for reasons to be demonstrated in Section 5.1.1.

In this paper, a set of 25 trigonometric functions are employed as the basis for KED to model a periodic trend m, namely,

$$\{f(\mathbf{x}) = \prod_{i=1}^{2} f_i(2\pi t^{(i)}) | f_1, f_2 \in \{1, \cos(t), \sin(t), \cos(2t), \sin(2t)\}\}, \tag{38}$$

where $t^{(i)}$ is the i-th term of $\mathbf{t} = \mathbf{P}^{-1} \cdot \mathbf{x}$, and $\mathbf{P}$ is the periodicity matrix of the surface. It should be noted that including as many as 25 trigonometric basis functions goes beyond standard practice. In most practices of KED, only low-order polynomials are used. Trigonometric kriging [51], another variant of KED, employs three terms for periodic 1-D signals. When applied to the spatial case, the regular trigonometric kriging includes $3 \times 3 = 9$ terms. However, compared to the 25-term version, it demonstrates significantly inferior performance as it lacks the ability to capture periodicity of higher frequencies. Theoretically, the computational complexity of the kriging estimator for FK is lower than that of KED. This is because KED involves solving a linear system, the computational time of which scales linearly with the number of basis functions. In the two case studies presented, this theoretical advantage is not significant due to numerical implementations; generally FK is only slightly faster than KED in solving corresponding linear systems.

In all situations standard isotropic covariance models are used. To make it sufficiently flexible for both FK and KED, we use the following additive model with five terms:

$$c(\mathbf{x}, \mathbf{x}') = c(\|\mathbf{x} - \mathbf{x}'\|) = \sum_{j=1}^{5} \lambda_j c_j(\|\mathbf{x} - \mathbf{x}'\|/l_j), \tag{39}$$

where

$$c_1(s) = \exp(-s),$$

$$c_2(s) = \exp(-s^2),$$

$$c_3(s) = c_{\text{Matern},\nu=3/2}(s) = (1 + \sqrt{3}s)\exp(-\sqrt{3}s),$$

$$c_4(s) = c_{\text{Matern},\nu=5/2}(s) = (1 + \sqrt{5}s + \frac{5}{3}s^2)\exp(-\sqrt{5}s),$$

$$c_5(s) = J_0(2\pi s).$$

J_0 in $c_5(s)$ is the ordinary Bessel function of the first kind of order 0, which can capture possible non-monotonic behavior as shown in [45]. We also assume no nuggets, because the surfaces are all continuous, and the low measurement noise may not be distinguished with small-scale variation.

5.1. Case study 1: TPL surface

TPL is a manufacturing technique for fabrication of three-dimensional complex micro/nanostructures with sub-nanometer resolution. In this study, we use measurements of five surfaces, on which there are 5×5 hemisphere structures manufactured with a Nanoscribe Photonic Professional GT 3D Printer, as shown in Figure 2. Each high-resolution measurement produces a 406×400 surface (94.8 nm between adjacent pixels). The distance between adjacent hemisphere centers is 7.5 µm by design with possible errors when manufactured.

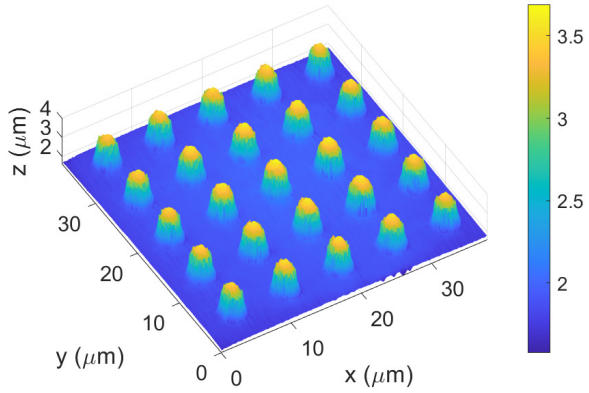

Figure 2: Hemisphere structures manufactured by TPL.

5.1.1. Difficulties with ordinary kriging

We first show why ordinary kriging is not applicable in this case. If a constant mean is assumed, the empirical covariance for spatial lags within 12.3 µm in each direction is shown in Figure 3(a). It is clear that the actual covariance in 2D is far from being isotropic, which explains why ordinary kriging is not applicable with isotropic covariance models. One may ignore these issues, map the graph of a 2-D function along the radial direction with $(x, y, f) \mapsto (r = \sqrt{x^2 + y^2}, f)$,

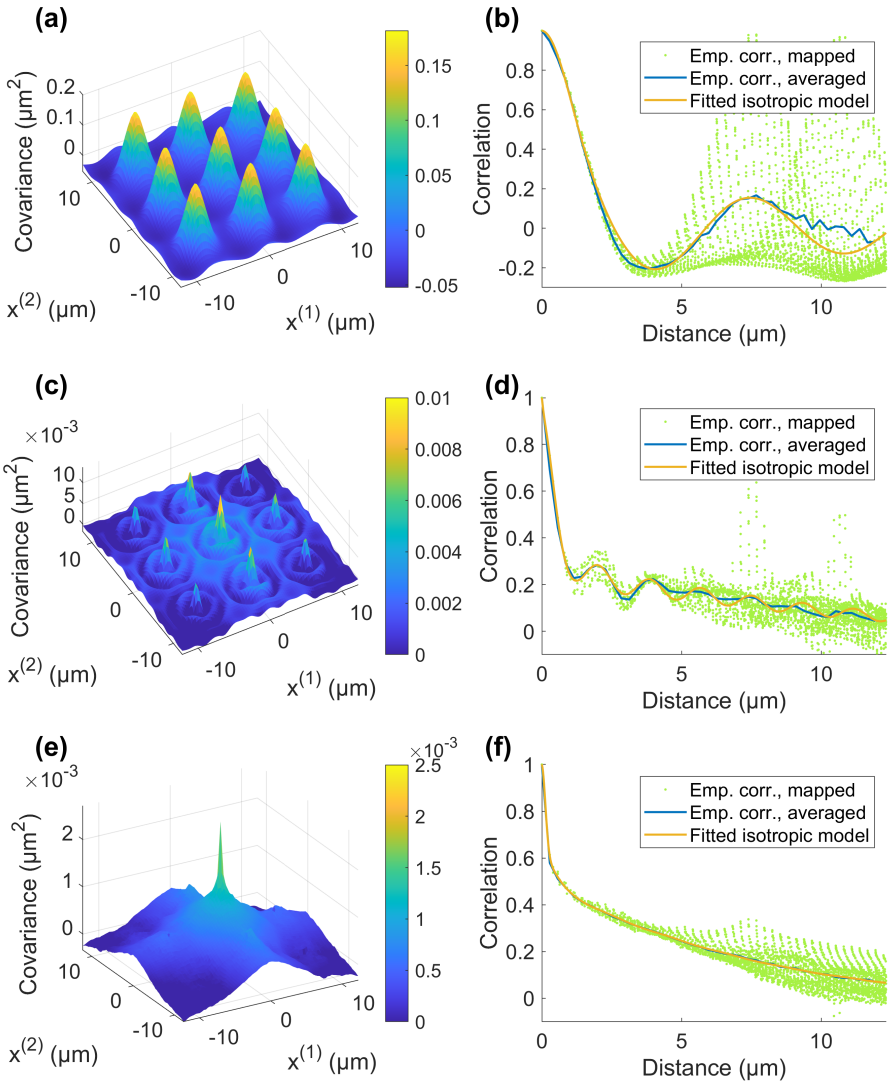

Figure 3: Empirical covariance of a TPL manufactured sample for (a) ordinary kriging, (c) KED, and (e) bicubic-FK. Empirical correlation for (b) ordinary kriging, (d) KED and (f) bicubic-FK when mapped along the radial direction, averaged and fitted.

and then take the weighted average for (nearly) equidistant points and fit an isotropic covariance model to it, as shown in Figure 3(b). Ordinary kriging could be performed with an isotropic model fitted this way; however, the result may depend heavily on the size of the kriging neighborhood, for which any large radius can cause both bad performance and numerical instability. It is also seen that the 2D empirical covariance is almost periodic with little decay, implying undesirable numerical difficulties with the inference because of multicollinearity, even if the covariance is accurately modeled at the cost of greater complexity.

Compared with ordinary kriging, the isotropy issue is largely eased for KED, as shown by its empirical covariance in Figure 3(c,d). Although the isotropy assumption is still violated by a residual periodic pattern, KED yields reasonable estimations with the isotropic model (39).

5.1.2. Settings for FK

To apply FK, we follow the procedure described in Sections 2 and 4. First, a filter is designed to suppress the periodic component. The periodicity matrix of the surface is $\mathbf{P} = \mathrm{diag}\{T_0, T_0\}$, where $T_0 \approx 7.5\,\mu\mathrm{m}$. The filter weights are produced using Eq. (30) with $w_{\mathbf{m}} = w_{1,m^{(1)}} w_{2,m^{(2)}}$, where $\mathbf{m} \in \{-2, -1, \ldots, 2\}^2$, $w_{i,m} = r \exp(-2(m/2)^2)$ for $i = 1, 2$, and r normalizes the sum of $w_{\mathbf{m}}$'s to be one. The periodicity matrix of the interpolation grid is $\mathbf{L}_0 = \mathrm{diag}\{l_0, l_0\}$, where $l_0 = 94.8\,\mathrm{nm}$. To avoid off-grid computation, let $T_0' = 79 l_0 = 7.49\mu m (\approx T_0)$, and $\mathbf{P}' = \mathrm{diag}\{T_0', T_0'\}$ is adopted to evaluate Eq. (37).

Then, bilinear and bicubic interpolation are used in the second step to produce h_{Int}. With the designed filter applied to h_{Int}, the periodic component in the residual H_{res} is largely reduced (see Figure 4). The empirical covariance of the residual is plotted in the Figure 3(e,f), which suggest that the correlation becomes mostly isotropic, and could be fitted more precisely with common isotropic models. The weight function in [52] is used in weighted least squares for covariance fitting.

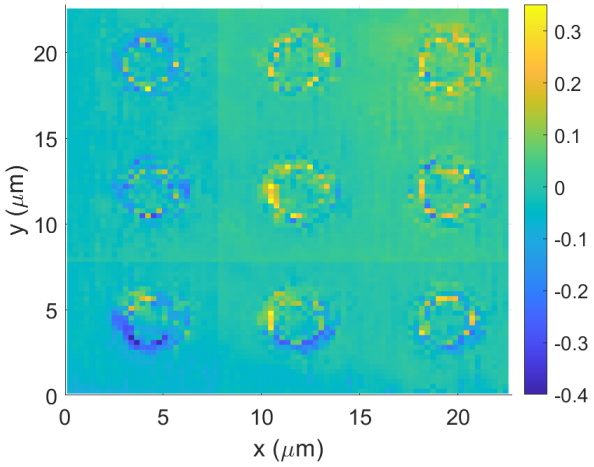

Figure 4: The residual Y_{res} after bicubic pre-interpolation and bandpass filtering.

5.1.3. Performance comparison

RMSE comparison is reported in Table 3 and Figure 5. It is shown that FK achieves the lowest prediction errors compared with KED, bicubic or bilinear interpolation alone for all samples. In most cases, FK works better with bicubic pre-interpolation than with bilinear.

Table 3: RMSE (nm) of the five interpolation methods for TPL data. The best results are marked boldface for each sample number and the average.

Sample No.	bicubic-FK	bilinear-FK	KED	bicubic	linear
1	**33.04**±0.33	33.08±0.29	34.22±0.36	34.12±0.27	34.61±0.39
2	**33.24**±0.23	33.34±0.24	34.15±0.15	34.38±0.17	34.66±0.20
3	**32.22**±0.14	32.57±0.17	33.24±0.28	33.38±0.15	33.84±0.17
4	**32.99**±0.30	33.26±0.32	34.17±0.28	34.37±0.24	34.87±0.25
5	36.27±0.30	**36.09**±0.26	37.18±0.36	37.10±0.21	37.63±0.23
Average	**33.552**	33.6674	34.5928	34.6716	35.1236

While FK makes improvement based on the pre-interpolation method selected, and better pre-processing tends to yield a better result, it is observed that different pre-interpolation methods are "leveled/evened" after filtering. This is expected because the difference between interpolation results generally has a spreading spectrum, and can be significantly weakened after passing a filter

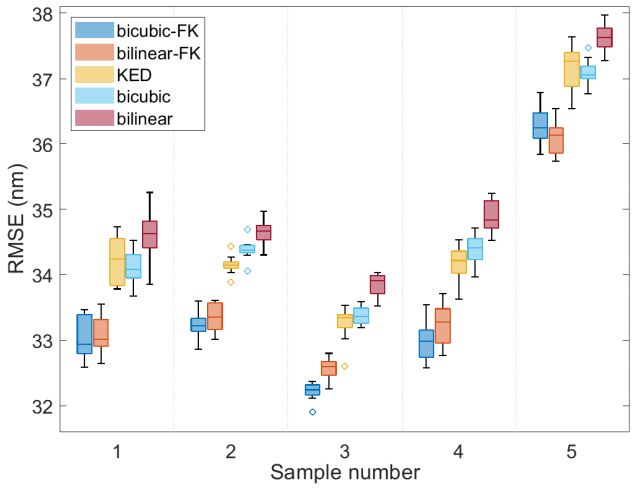

Figure 5: RMSE of the five interpolation methods for TPL data.

with a narrow total bandwidth.

5.2. Case study 2: UMW tool surface

The data in this case study contains surface measurements of UMW anvils in different life stages [17]. Degradation of anvil surfaces could affect the joint quality strongly [44]. Each original high-resolution measurement ($l_0 = 22.032\,\mu\text{m}$ per pixel) produces a 163×900 surface. The 3D height plots are shown in Figure 6.

Knurls are located on the anvil with periodicity matrix

$$\mathbf{P} = T_0 \cdot \begin{pmatrix} 1/2 & 1/2 \\ -1/2 & 1/2 \end{pmatrix}, \tag{40}$$

where $T_0 = 1.436\text{mm}$.

Figure 7 shows the empirical covariance of surface 3. A bandpass filter is designed following the same methodology. Implementation details are presented in Section **??** of the SI. Both bicubic and bilinear methods are used for pre-interpolation. Empirical covariance computed from the filtered residual of bicubic-FK is shown in Figure 7 (e,f).

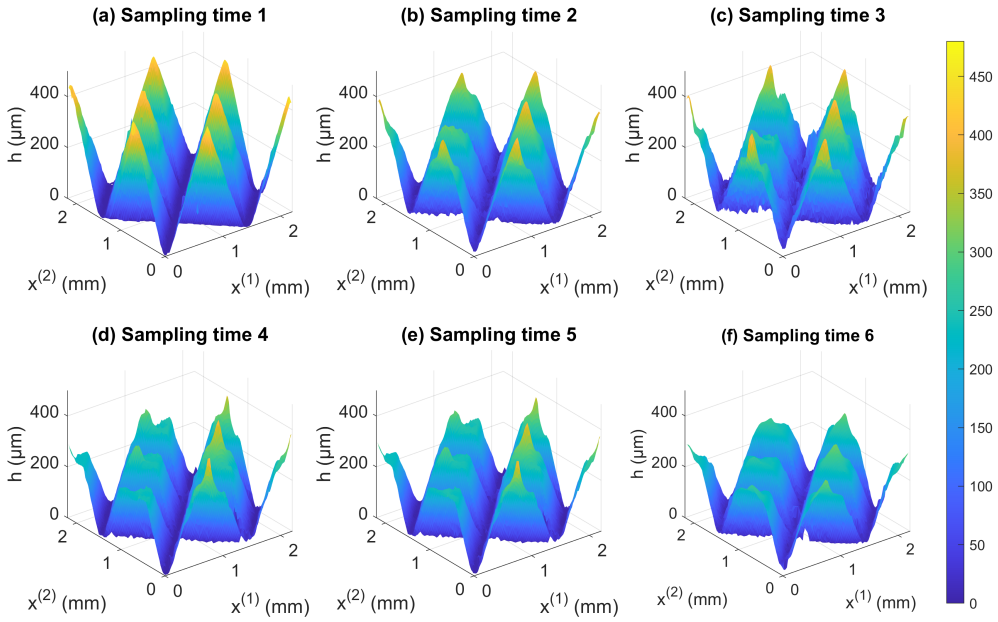

Figure 6: Six measurements of an anvil surface in UMW.

RMSE is summarized and compared in Table 4 and Figure 8. Again, the lowest prediction RMSE is achieved by the FK with bicubic pre-interpolation for all sampling times. More significantly than in the TPL case, the difference between bicubic and bilinear pre-interpolation are reduced after the FK procedure.

Table 4: RMSE (μm) of the five interpolation methods for UMW anvil data. The best results are marked boldface for each sampling time and the average.

Surface No.	bicubic-FK	bilinear-FK	KED	bicubic	bilinear
1	**4.392**±0.073	4.480±0.083	4.835±0.046	4.689±0.078	5.517±0.103
2	**4.079**±0.028	4.135±0.036	4.296±0.041	4.286±0.048	5.097±0.062
3	**7.485**±0.033	7.603±0.032	7.675±0.043	7.802±0.050	8.192±0.046
4	**5.455**±0.073	5.515±0.082	5.549±0.078	5.576±0.085	6.397±0.092
5	**4.724**±0.062	4.785±0.074	4.816±0.066	4.852±0.077	5.731±0.086
6	**3.814**±0.024	3.879±0.030	3.920±0.029	3.970±0.032	4.815±0.035
Average	**4.9915**	5.0661	5.1818	5.1957	5.9583

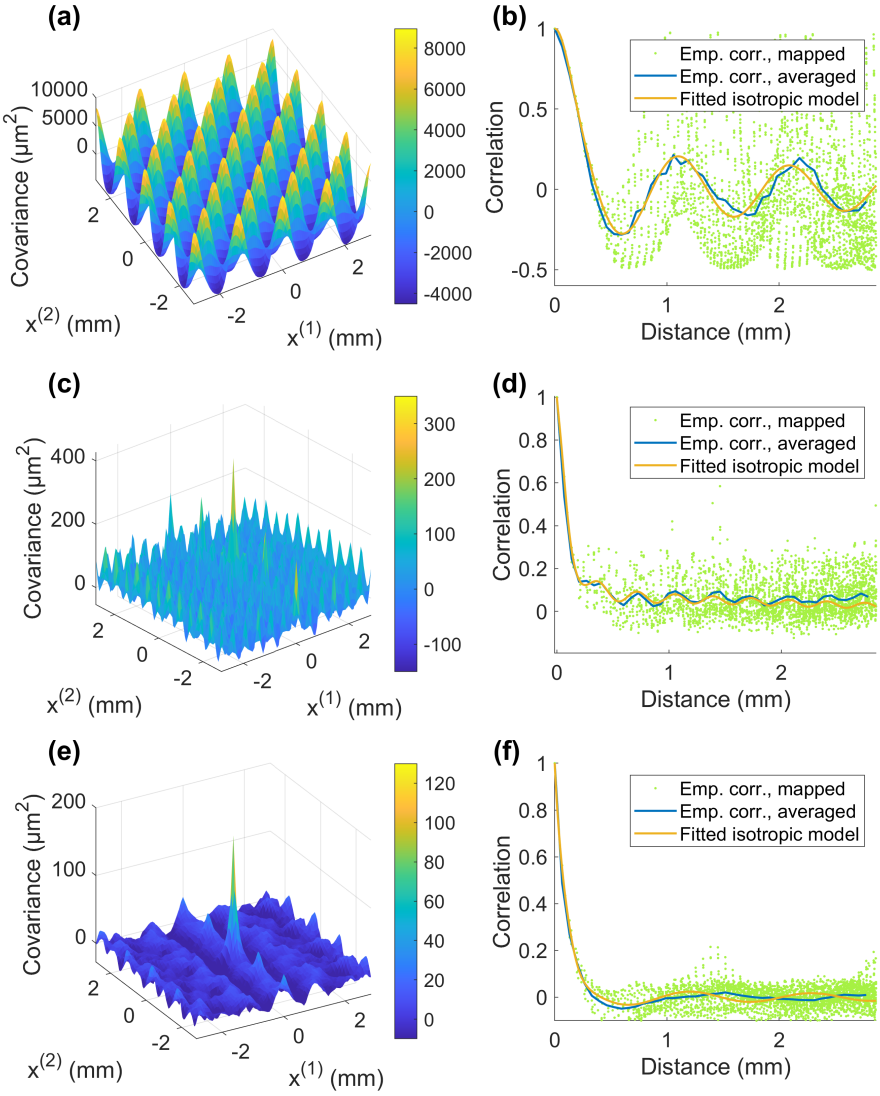

Figure 7: Empirical covariance of the UMW tool surface at sampling time 3 for (a) ordinary kriging, (c) KED, and (e) bicubic-FK. Empirical correlation for (b) ordinary kriging, (d) KED and (f) bicubic-FK mapped along the radial direction, averaged and fitted.

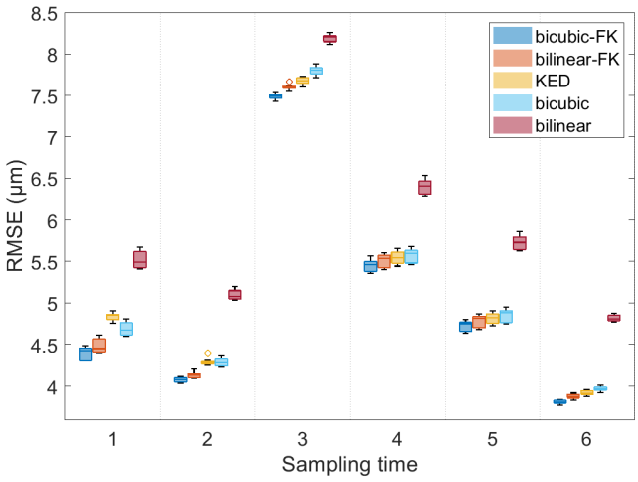

Figure 8: RMSE of the five interpolation methods for UMW surfaces.

6. Conclusion

Modeling of periodic surfaces with kriging or Gaussian process regression has been challenging in the past because of complicated covariance structures. In this paper, we propose the FK procedure to enhance the conventional kriging-type methods with a pre-filtering step. With the FK technique that adopts a bandpass filter, common isotropic models become applicable to periodic surfaces with improved goodness-of-fit and interpolation accuracy, with potential numerical issues alleviated. Through analysis using frequency domain techniques, the mechanisms of the FK method are illustrated both qualitatively and quantitatively, and conditions for effective pre-filtering are identified. Within this analytical framework, a new theorem is proven that establishes the equivalence between kriging estimation and the perfect reconstruction from alias-free measurements, as guaranteed by the Nyquist-Shannon sampling theorem. Based on derived conditions, a practical bandpass filter design for periodic surfaces and its implementation are demonstrated. The effectiveness of FK and the filter design strategy is verified with two real-world manufacturing case studies, showing superior interpolation performance compared to state-of-the-art methods.

As a final remark, it is noteworthy that the core principle of FK is to iso-

late challenging components without significant extra cost, while leaving the readily manageable part undisturbed. This inherently does not rely on uniform sampling, linear pre-interpolation, convolutional filtering and process with periodicity, which are required for rigorous quantitative analysis. Consequently, FK can potentially be applied to a wider range of filters and processes, opening the possibility of leveraging various signal processing techniques to address spatial problems.

Acknowledgments

This research has been supported by the National Science Foundation, USA under Grants No. 1944345, and No. 2043168, No. 2433484, and No. 2434813. The TPL experiments were carried out in the Materials Research Laboratory Central Research Facilities, University of Illinois.

References

[1] Rahul A. Mali, T. V. K. Gupta, and J. Ramkumar. A comprehensive review of free-form surface milling– Advances over a decade. *Journal of Manufacturing Processes*, 62:132–167, February 2021.

[2] Yaxiang Yin, Yiping Shao, Kun Wang, Shichang Du, and Lifeng Xi. Segmentation of workpiece surfaces with tool marks based on high definition metrology. *Journal of Manufacturing Processes*, 57:268–287, September 2020.

[3] Yang Cao, Xuesen Zhao, Guo Li, Wenjun Zong, and Tao Sun. Study regarding the influence of process conditions on the surface topography during ultra-precision turning. *Journal of Manufacturing Processes*, 102:23–36, September 2023.

[4] Xinchen Wang, Mohammad Alshoul, Huimin Zhou, Jia Deng, and Zimo Wang. Study of the system instability impacts on surface characteristics for vibration-assisted AFM-based nanomachining. *Journal of Manufacturing Processes*, 117:213–223, May 2024.

[5] Jia Peter Liu, Ran Jin, and Zhenyu James Kong. Wafer quality monitoring using spatial Dirichlet process based mixed-effect profile modeling scheme. *Journal of Manufacturing Systems*, 48:21–32, July 2018.

[6] Xin Liu, Bingqi Wang, Yuheng Li, Yuyang Zhou, Jiahao Zhang, Ziheng Wang, Jingcan Yan, Xiaolei Gu, Zizhen Yuan, Yang Chen, Shuaishuai Wang, and Jiyu Liu. Improving machinability of single-crystal silicon by cold plasma jet. *Journal of Manufacturing Processes*, 99:581–591, August 2023.

[7] Haotian Chen, Yuhang Yang, and Chenhui Shao. Multi-task learning for data-efficient spatiotemporal modeling of tool surface progression in ultrasonic metal welding. *Journal of Manufacturing Systems*, 58:306–315, January 2021.

[8] Yuhang Yang, Yifang Zhang, Y. Dora Cai, Qiyue Lu, Seid Koric, and Chenhui Shao. Hierarchical measurement strategy for cost-effective interpolation of spatiotemporal data in manufacturing. *Journal of Manufacturing Systems*, 53:159–168, October 2019.

[9] Yuhang Yang, Varun A. Kelkar, Hemangg S. Rajput, Adriana C. Salazar Coariti, Kimani C. Toussaint, and Chenhui Shao. Machine-learning-enabled geometric compliance improvement in two-photon lithography without hardware modifications. *Journal of Manufacturing Processes*, 76:841–849, April 2022.

[10] Sixian Jia, Jieliyue Sun, Andrew Howes, Michelle R Dawson, Kimani C Toussaint Jr, and Chenhui Shao. Hybrid physics-guided data-driven modeling for generalizable geometric accuracy prediction and improvement in two-photon lithography. *Journal of Manufacturing Processes*, 110:202–210, 2024.

[11] Andrew Townsend, Nicola Senin, Liam Blunt, RK Leach, and JS Taylor. Surface texture metrology for metal additive manufacturing: a review. *Precision Engineering*, 46:34–47, October 2016.

[12] Xiao Zhang, Yi Zheng, Vignesh Suresh, Shaodong Wang, Qing Li, Beiwen Li, and Hantang Qin. Correlation approach for quality assurance of additive manufactured parts based on optical metrology. *Journal of Manufacturing Processes*, 53:310–317, May 2020.

[13] Pablo Gamonal-Repiso, Miguel Sánchez-Soto, Soledad Santos-Pinto, and Maria Lluïsa Maspoch. Improvement of the replication quality of randomly micro-textured injection-moulding components using a multi-scale surface analysis. *Journal of Manufacturing Processes*, 42:67–81, June 2019.

[14] Ali Heidarinejad and Fakhreddin Ashrafizadeh. Influence of surface texture and coating thickness on adhesion of nickel plated coatings to aluminium substrate. *Journal of Manufacturing Processes*, 120:435–448, June 2024.

[15] M. Roeder, S. Thiele, D. Hera, C. Pruss, T. Guenther, W. Osten, and A. Zimmermann. Fabrication of curved diffractive optical elements by means of laser direct writing, electroplating, and injection compression molding. *Journal of Manufacturing Processes*, 47:402–409, November 2019.

[16] Yuhang Yang, Zhiqiao Dong, Yuquan Meng, and Chenhui Shao. Data-Driven Intelligent 3D Surface Measurement in Smart Manufacturing: Review and Outlook. *Machines*, 9(1):13, January 2021.

[17] Chenhui Shao, Jionghua Judy Jin, and S Jack Hu. Dynamic sampling design for characterizing spatiotemporal processes in manufacturing. *Journal of Manufacturing Science and Engineering*, 139(10), 2017.

[18] Pascal Getreuer. Linear Methods for Image Interpolation. *Image Processing On Line*, 1:238–259, September 2011.

[19] Isaac Amidror. Scattered data interpolation methods for electronic imaging systems: a survey. *Journal of electronic imaging*, 11(2):157–176, 2002.

[20] Alan E. Gelfand, Peter Diggle, Peter Guttorp, and Montserrat Fuentes. *Handbook of Spatial Statistics*. CRC Press, March 2010.

[21] Christopher KI Williams and Carl Edward Rasmussen. *Gaussian processes for machine learning*, volume 2. MIT press Cambridge, MA, 2006.

[22] Jingwei Bai, Xing Zhong, Shan Jiang, Yu Huang, and Xiangfeng Duan. Graphene nanomesh. *Nature Nanotechnology*, 5(3):190–194, March 2010.

[23] Volker C. Radeloff, Todd F. Miller, Hong S. He, and David J. Mladenoff. Periodicity in Spatial Data and Geostatistical Models: Autocorrelation between Patches. *Ecography*, 23(1):81–91, 2000.

[24] Erchan Aptoula. Remote Sensing Image Retrieval With Global Morphological Texture Descriptors. *IEEE Transactions on Geoscience and Remote Sensing*, 52(5):3023–3034, May 2014.

[25] Hai Trong Nguyen, Hui Wang, and S. Jack Hu. Modeling cutter tilt and cutter-spindle stiffness for machine condition monitoring in face milling using high-definition surface metrology. *The International Journal of Advanced Manufacturing Technology*, 70(5):1323–1335, February 2014.

[26] V. L. Zakovorotnyi and V. E. Gvindjiliya. Influence of speeds of forming movements on the properties of geometric topology of the part in longitudinal turning. *Journal of Manufacturing Processes*, 112:202–213, February 2024.

[27] Woo-Jong Yeo, Hwan-Jin Choi, Minwoo Jeon, Mincheol Kim, Young-Jae Kim, Byeong Joon Jeong, Seok-Kyeong Jeong, Jong-Gyun Kang, Dong-Ho Lee, Geon-Hee Kim, I Jong Kim, and Wonkyun Lee. Enhancement of optical surface quality based on real-time compensation of temperature-driven thermal errors in diamond turning. *Journal of Manufacturing Processes*, 110:424–433, January 2024.

[28] Giacomo Maculotti, Giovanni Pistone, and Grazia Vicario. Inference on errors in industrial parts: Kriging and variogram versus geometrical product specifications standard. *Applied Stochastic Models in Business and Industry*, 37(5):839–858, 2021.

[29] Qi Jialiang, Gao Hang, Wang Yiqi, Li Lun, and Xiao Shenglei. Research on the surface flattening model for carbon fiber plain-woven composite preforming processing. *Journal of Manufacturing Processes*, 69:223–234, September 2021.

[30] C. M. H. Hagen, A. Hognestad, O. Ø. Knudsen, and K. Sørby. The effect of surface roughness on corrosion resistance of machined and epoxy coated steel. *Progress in Organic Coatings*, 130:17–23, May 2019.

[31] Kodai Nagayama and Jiwang Yan. Deterministic error compensation for slow tool servo-driven diamond turning of freeform surface with nanometric form accuracy. *Journal of Manufacturing Processes*, 64:45–57, April 2021.

[32] Bo Xue, Chunmei Yang, Yanquan Geng, and Yongda Yan. A novel fabrication of micro/nano hierarchical grating structures for structural coloration by using revolving tip-based machining method. *Journal of Manufacturing Processes*, 62:202–212, February 2021.

[33] Tianfeng Zhou, Jia Zhou, Tianxing Wang, Liheng Gao, Benshuai Ruan, Qian Yu, Wenxiang Zhao, and Xibin Wang. Fabrication of high aspect-ratio aspheric microlens array based on local spiral diamond milling. *Journal of Manufacturing Processes*, 83:547–554, November 2022.

[34] Jieliyue Sun, Andrew M. Howes, Sixian Jia, Joshua A. Burrow, Pedro F. Felzenszwalb, Michelle R. Dawson, Chenhui Shao, and Kimani C. Toussaint. Automated brightfield layerwise evaluation in three-dimensional micropatterning via two-photon polymerization. *Opt. Express*, 32(7):12508–12519, Mar 2024.

[35] Adrian H. A. Lutey, Gianmarco Lazzini, Laura Gemini, Alexander Peter, Volkher Onuseit, Javier Graus, Francesco Fuso, Rainer Kling, and Luca Romoli. Insight into replication effectiveness of laser-textured micro and nanoscale morphology by injection molding. *Journal of Manufacturing Processes*, 65:445–454, May 2021.

[36] Mert Gülçür, Elaine Brown, Tim Gough, and Ben Whiteside. Characterisation of microneedle replication and flow behaviour in ultrasonic microinjection moulding through design of experiments. *Journal of Manufacturing Processes*, 102:513–527, September 2023.

[37] Hojun Na, Jeonghyun Yoo, and Hyungson Ki. Prediction of surface morphology and reflection spectrum of laser-induced periodic surface structures using deep learning. *Journal of Manufacturing Processes*, 84:1274–1283, December 2022.

[38] Bo Mao, Arpith Siddaiah, Yiliang Liao, and Pradeep L. Menezes. Laser surface texturing and related techniques for enhancing tribological performance of engineering materials: A review. *Journal of Manufacturing Processes*, 53:153–173, May 2020.

[39] Hansong Chen, Zongbao Shen, Pin Li, and Lei Zhang. Fabrication of homogeneous multiscale microtexture surfaces on copper foil by laser shock imprinting with two-step overlapping laser shock path. *Journal of Manufacturing Processes*, 86:10–29, January 2023.

[40] Huimin Wang, Daxiang Deng, Zhenjie Zhai, and Yingxue Yao. Laser-processed functional surface structures for multi-functional applications-a review. *Journal of Manufacturing Processes*, 116:247–283, April 2024.

[41] Yu Guo and Haibin Zhao. Femtosecond laser processed superhydrophobic surface. *Journal of Manufacturing Processes*, 109:250–287, January 2024.

[42] A. Fouathiya, S. Meziani, M. Sahli, and T. Barrière. Experimental investigation of microtextured cutting tool performance in titanium alloy via turning. *Journal of Manufacturing Processes*, 69:33–46, September 2021.

[43] Avik Samanta, Qinghua Wang, Gurjap Singh, Scott K. Shaw, Fatima Toor, Albert Ratner, and Hongtao Ding. Nanosecond pulsed laser processing turns engineering metal alloys antireflective and superwicking. *Journal of Manufacturing Processes*, 54:28–37, June 2020.

[44] Chenhui Shao, Tae Hyung Kim, S Jack Hu, Jionghua Jin, Jeffrey A Abell, and J Patrick Spicer. Tool wear monitoring for ultrasonic metal welding of lithium-ion batteries. *Journal of Manufacturing Science and Engineering*, 138(5), 2016.

[45] Yuhang Yang and Chenhui Shao. Spatial interpolation for periodic surfaces in manufacturing using a bessel additive variogram model. *Journal of Manufacturing Science and Engineering*, 140(6), 2018.

[46] Holger Wendland. *Scattered Data Approximation*. Cambridge University Press, December 2004.

[47] Robert Marks. *Introduction to Shannon Sampling and Interpolation Theory*. Springer Texts in Electrical Engineering. Springer-Verlag, New York, 1991.

[48] Robert J. Adler. *Random fields and geometry*. Number 115 in Springer monographs in mathematics. Springer, New York, 2007.

[49] Michael Scheuerer. Regularity of the sample paths of a general second order random field. *Stochastic Processes and their Applications*, 120(10):1879–1897, September 2010.

[50] Peter J Brockwell and Richard A Davis. *Time series: theory and methods*. Springer Science & Business Media, 2009.

[51] Serge Seguret and Philippe Huchon. TrigonometricK riging: A New Methodf or Removingt he Diurnal Variation From Geomagnetic Data. *Journal of Geophysical Research: Solid Earth*, 95(B13):21383–21397, 1990.

[52] X. F. Zhang, J. C. H. Van Eijkeren, and A. W. Heemink. On the weighted least-squares method for fitting a semivariogram model. *Computers & Geosciences*, 21(4):605–608, May 1995.